ELSEVIER

Journal of Nuclear Materials 313–316 (2003) 1141–1149

journal of nuclear materials

www.elsevier.com/locate/jnucmat

Impact of $\vec{E} \times \vec{B}$ drifts on the distribution of impurities in the Tokamak plasma edge

V. Rozhansky [a,*], E. Kaveeva [a], S. Voskoboynikov [a], A.H. Bekheit [a], D. Coster [b], X. Bonnin [c], R. Schneider [c]

[a] St. Petersburg State Technical University, Polytechnicheskaya 29, 195251 St. Petersburg, Russia
[b] Max-Planck Institut fur Plasmaphysik, Euroatom Association, D-85748 Garching, Germany
[c] Max-Planck Institut fur Plasmaphysik, Teilinstitut Greifswald, Euroatom Association, D-17491 Greifswald, Germany

Received 27 May 2002; accepted 12 September 2002

Abstract

The impurity transport in the edge plasma of a divertor tokamak is simulated by means of B2-SOLPS5.0 2D multi-fluid code where diamagnetic and $\vec{E} \times \vec{B}$ drifts for all species are taken into account. It is demonstrated that these drifts to large extent determine the poloidal distribution of impurities near the separatrix and hence penetration of impurities to the core region. The influence of the drifts on the low ionized impurity distribution in the divertor region is more modest.

PACS: 52.25.Fi
Keywords: Plasma-wall interactions; Divertor; Boundary plasmas; Carbon; Recycling; B2-SOLPS5.0

1. Introduction

As well-known impurity transport in the divertor region of a tokamak and impurity penetration to the core is one of the key issues in the edge plasma physics [1]. According to the simple 1D analysis the three forces determine the parallel (poloidal) flux of impurities in the divertor: friction with the background ions, pressure gradient and thermal force. The leakage or retention of impurities is governed by the balance between these forces (see [1] and references therein). Many authors discussed also 1D model of penetration of impurities in the region inside the separatrix. Here the radial velocity of impurities is determined by the neoclassical effect [2] and by anomalous diffusion and convection. In reality the impurity distribution in the edge plasma is essentially two-dimensional and 2D code should be used to analyze the problem. Series of simulations for ASDEX-Upgrade tokamak were performed with the B2 transport code [3] where the fluid equations were solved with perpendicular transport coefficients replaced by their anomalous values. It was demonstrated that the impurity distribution in the divertor region is consistent with the experiments. However, effects connected with $\vec{E} \times \vec{B}$ and diamagnetic drifts, which in principle may change the impurity flow pattern, were not included in this version of the code.

In the present paper the impurity transport in the edge plasma is simulated by means of B2-SOLPS5.0 2D multi-fluid code [4], where the most complete system of transport equations including diamagnetic and $\vec{E} \times \vec{B}$ drifts is solved for all species. It is shown that these drifts to large extent determine the poloidal distribution of impurities near the separatrix and hence their penetration to the core region. The influence of the drifts on the low ionized impurity distribution in the divertor region is more modest.

2. Simulation results

The simulations were performed for the typical L-regimes of the ASDEX-Upgrade (AUG): $I = 1$ MA,

* Corresponding author. Tel./fax: +1-812 552 7954.
E-mail address: rozhansky@phtf.stu.neva.ru (V. Rozhansky).

0022-3115/03/$ - see front matter
PII: S0022-3115(02)01578-7

$B = 2$ T, the density in the reference point located at $a - r = 1$ cm (a is the radial co-ordinate of the separatrix) at the equatorial midplane $n_e = 2 \times 10^{19}$–2.7×10^{19} m^{-3}, the ion (deuterium) temperature $T_i = 40$–100 eV. As an impurity the carbon was chosen. The anomalous values of diffusion and heat conductivity coefficients were chosen equal for the all sorts of particles: $D = 0.5$ m^2/s; $\chi_{e,i} = 0.7$ m^2/s. The impurity source was determined by the chemical sputtering at the material surfaces with the sputtering yield $\gamma = 1$–3%. Several calculations were made with the drifts switched on and off for the investigation of their role in impurity redistribution.

The computational domain and the coordinates are shown in Fig. 1, x is the poloidal coordinate directed from the inner to the outer plate in the scrape-off layer (SOL) and from the inner to the outer plate in the private flux region (PFR). The ∇B drift of ions is directed towards the X-point. The typical profile of the radial electric field in the presence of impurities is almost the same as was calculated in the absence of impurities in [4], Fig. 2. The radial electric field is compared with the neoclassical prediction and one can see that the field calculated in the code is close to the neoclassical one on the closed flux surfaces. It is also consistent with the measurements on DIII-D and other tokamaks [4]. On the open field lines the potential is determined by the parallel momentum balance equation for electrons, and the radial electric field is positive. The profile of radiation losses with all the drifts switched on is rather typical and does not deviate significantly from that obtained in the runs without drifts. The examples of density profiles for different ionization states are shown in Fig. 3. One can see that the pattern of the impurity distribution is much more complicated than in the simple 1D model. First of all for the regimes chosen noticeable part of the carbon neutrals penetrates up to the X-point, Fig. 3(a). Below the X-point carbon ionizes up to C^{1+}–C^{3+}, Fig. 3(b), diffuses in the radial direction across the flux surfaces and flows back to the divertor plates due to the friction with the background ions. In the absence of drifts the main processes, which determine the impurity density distribution, are the friction with deuterium ions

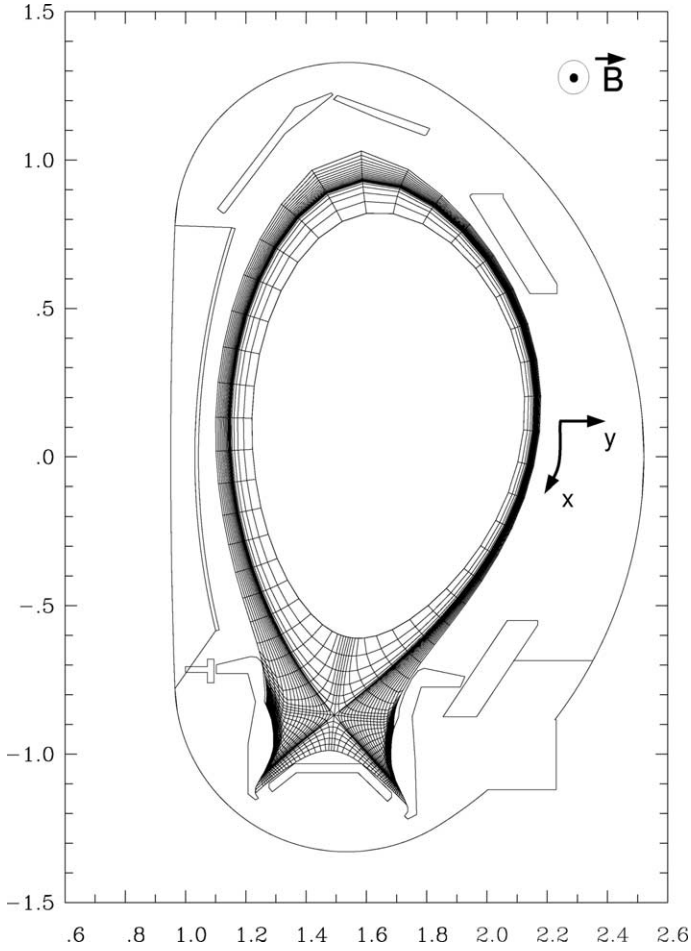

Fig. 1. Computation domain and coordinate system.

and perpendicular diffusion, while the thermal force and parallel diffusion of impurities with respect to the background ions are less significant. However, in the region of the steep temperature gradient near the outer divertor plate the contribution of thermal force is responsible for the poloidal inhomogeneity in C^{3+}. Switching off the drifts did not change significantly the distribution of low ionization states, Fig. 4, on average the difference is of the order of 10%. The poloidal distribution, Fig. 4, is presented for the representative flux surface in the SOL located 5 mm outside the separatrix in the equatorial midplane. The x-axis is directed clockwise. Note the break in the x-axis above the X-point, where the C^{3+} density is low. The impact of the $\vec{E} \times \vec{B}$ drifts on the C^{1+} and C^{2+} is even weaker than on C^{3+} distribution.

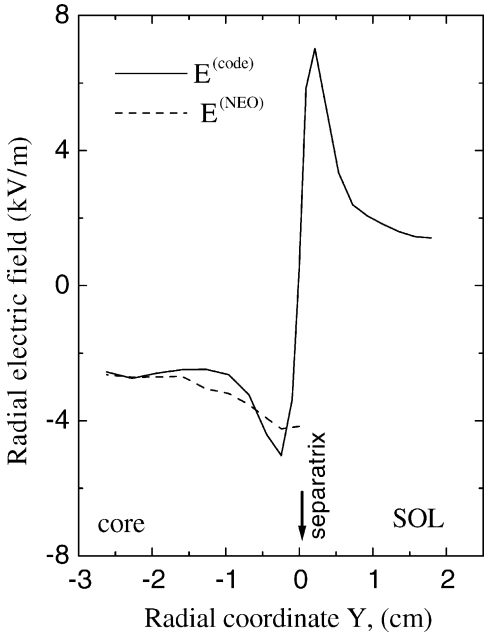

Fig. 2. Radial electric field at the equatorial midplane. By dashed line shown is the neoclassical electric field calculated in accordance with [4]. The discharge parameters are: $P = 1$ MW, $n_e|_{-1\ \mathrm{cm}} = 2.3 \times 10^{19}$ m^{-3}, without NBI.

The $\vec{E} \times \vec{B}$ drift of impurities in combination with the perpendicular anomalous diffusion should in principle result in change of their poloidal distribution. One would expect the reduction of their density and more gradual poloidal profile in the presence of drifts in the inner divertor leg and build up of the impurity density and steeper poloidal profile in the outer leg [5]. In the PFR more gradual poloidal profile in the outer divertor leg and steeper one in the inner divertor leg may be expected. However, this effect is not strong. The predicted influence of the $\vec{E} \times \vec{B}$ drifts may be noticed only very close to the separatrix. The explanation of this result consists in the role of the parallel flux of the background ions, which is different in the presence of the $\vec{E} \times \vec{B}$ drifts.

To understand the role of various fluxes the directions of the $\vec{E} \times \vec{B}$ drifts, poloidal and parallel fluxes are presented in the schematic Fig. 5 for normal direction of

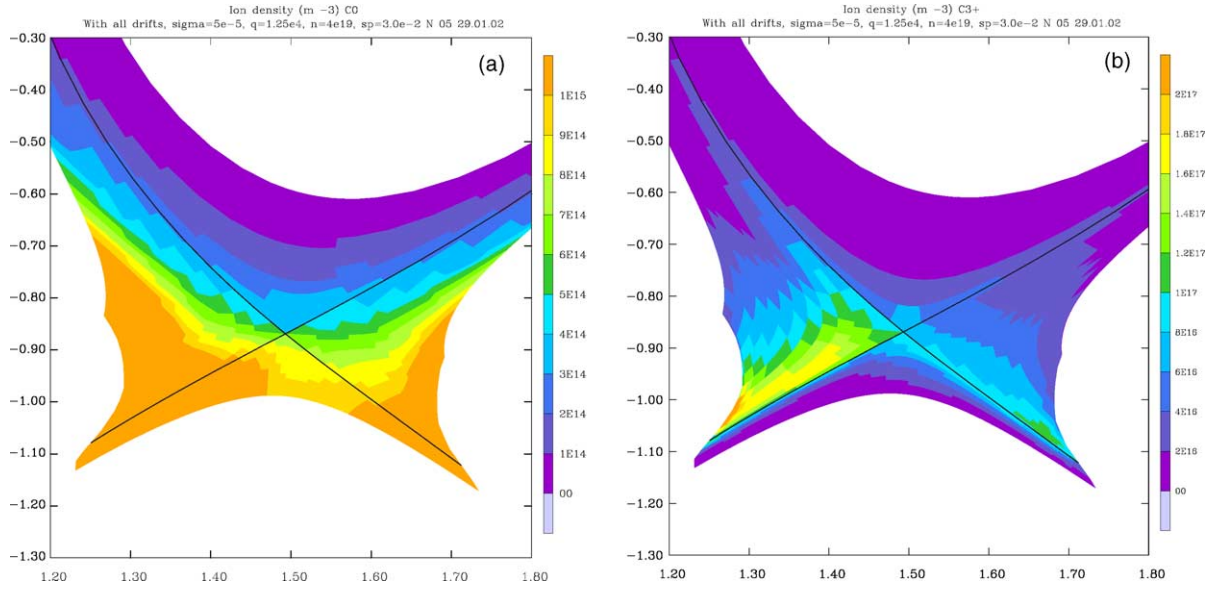

Fig. 3. (a) Distribution of the neutral carbon for the discharge parameters $P = 1$ MW, $n_e|_{-1\ \mathrm{cm}} = 2.3 \times 10^{19}$ m^{-3}, $Z_{\mathrm{eff}} = 1.4$. (b) Distribution of C^{3+}, the same parameters.

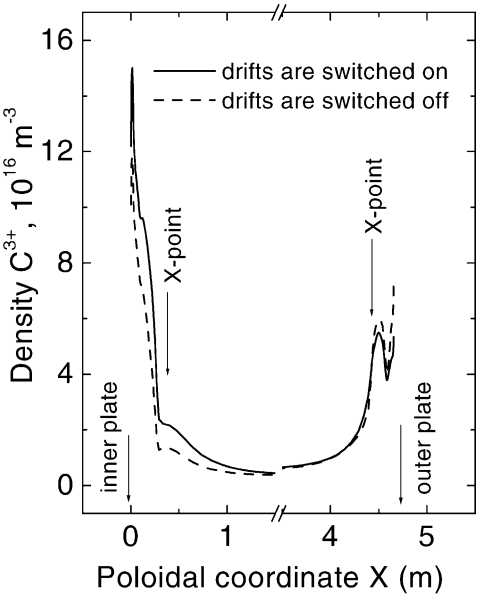

Fig. 4. Poloidal distributions of C^{3+} in the SOL with and without drifts. The position of X-point is shown. The x-coordinate is broken, the top coordinate is 2.26 m, the equatorial midplane is located at 3.10 m.

the magnetic field. The drift pattern in Fig. 5(a) corresponds to the calculated radial electric field, Fig. 2, and the maximum of the potential near the separatrix, for further details see [4]. As known from the simulations [4,6–8], the parallel fluxes of the background ions are significantly different in the presence of $\vec{E} \times \vec{B}$ drifts. Indeed, as was demonstrated in these publications, the parallel velocity, roughly speaking, changes in such a way that the total poloidal velocity (poloidal projection of the parallel velocity plus poloidal $\vec{E} \times \vec{B}$ drift) remains almost the same as without drifts, see Fig. 5(b). The reason is that the poloidal fluxes of the background ions, which close the radial fluxes from the core, should remain the same. The change in the parallel flux when the drifts are switched on is illustrated by Fig. 6 for the representative flux surface in the SOL located 5 mm outside the separatrix in the equatorial midplane. One can see the shift of stagnation point for the parallel velocity towards the outer midplane in the presence of drifts. The poloidal modulation of the parallel velocity is caused by the Pfirsch–Schlueter flux, which closes the diamagnetic drift of ions. The parallel flux of ions from the outer to the inner plate has been observed on JET [9] and JT-60 [10] with the stagnation point shifted from the top towards the outer midplane. Moreover, special experiments were performed on TdeV [11], where the radial electric field in the SOL was changed due to the target biasing, and the simultaneous change of the parallel velocity has been reported. The effect of the poloidal $\vec{E} \times \vec{B}$ drift compensation by the poloidal projection of the parallel flow was reported also in [12].

Hence, on one side, part of the impurity poloidal velocity changes due to the same $\vec{E} \times \vec{B}$ drift as that of the background ions but on the other side, impurity parallel velocity also changes due to the drag of the background ions in the opposite direction. As a result the total poloidal velocity of impurities remains almost the same. This fact explains the modest changes in the low ionized impurity distributions when the $\vec{E} \times \vec{B}$ drifts are switched on. Of course this is a simplified picture,

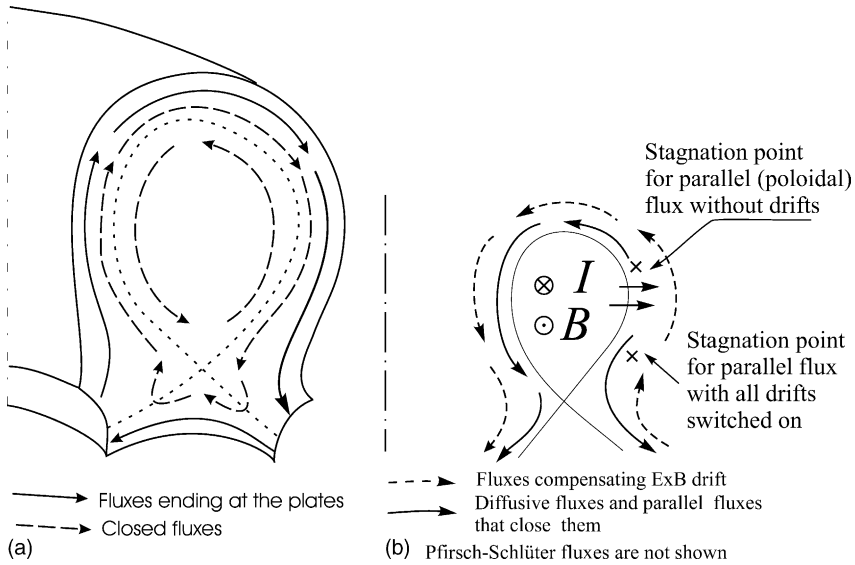

Fig. 5. Scheme of the fluxes of the background ions: (a) $\vec{E} \times \vec{B}$ drifts, (b) parallel, poloidal and diffusive fluxes (the latter are significantly larger through the outer part of the flux surface).

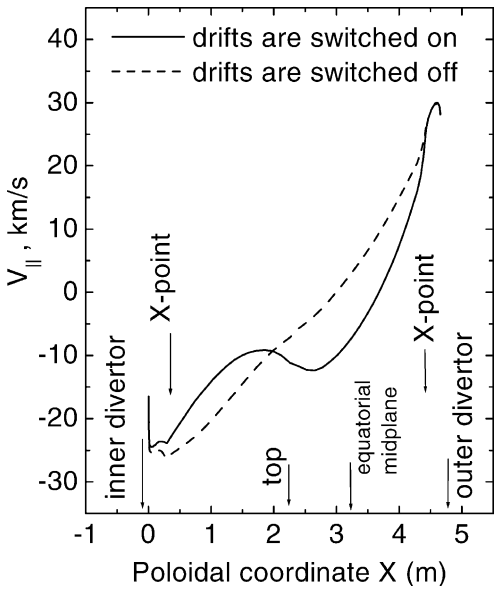

Fig. 6. Parallel velocity in the SOL with and without drifts.

since the impurity parallel velocity in the SOL deviates from that of the background ions. The exception is the open field lines very close to the separatrix. Here the poloidal $\vec{E} \times \vec{B}$ drifts do not end at the plates but are closed by the radial $\vec{E} \times \vec{B}$ drifts, so they are almost divergence free. Hence the parallel fluxes of the background ions do not compensate them and the effect of the drifts on the poloidal distribution of impurities is more pronounced. We neglect in our discussion (but not in the simulations) the dragging effect of impurities on the background ions. This is justified since in our cases the ratio of background to impurity densities exceeds the ratio of impurities mass to the mass of background ions by a factor 5–6 or larger.

Quite different is the situation for the higher ionization states on the closed flux surfaces inside the separatrix. Higher ionization states of carbon (C^{4+}, C^{5+}, C^{6+}) are born mainly inside the separatix due to successive ionization of neutral carbon. In particular, the source of C^{4+} (the fraction of C^{3+} inside the separatrix) is localized in the lower part of the flux surface in the vicinity of the X-point, Fig. 3(b). When the drifts are switched off the maximum of C^{4+} density corresponds to this region, Figs. 7 and 8. The poloidal width of the maximum of C^{4+} distribution is determined by the poloidal (parallel) and radial diffusion and by the distribution of C^{3+} (the source). In other words, the ions of C^{4+} diffuse both parallel to the magnetic field with respect to the background ions and in the radial direction until they cross the separatrix and start to move towards the plates together with the background ions, Fig. 9(a).

When the drifts are switched on the more uniform distribution of C^{4+} is observed, Figs. 7 and 8. The influence of ∇B drifts is not so pronounced as the influence of $\vec{E} \times \vec{B}$ drifts. This can be understood from the fact the radial electric field is of the order of neoclassical field [4,6]. In such a field $\vec{E} \times \vec{B}$ drifts and ∇B drifts give the contributions of the same order to the particle balance of the main component. Since ∇B drift velocity is proportional to Z^{-1} its contribution to the particle balance of C^{4+} is more modest than the contribution of $\vec{E} \times \vec{B}$ drift, which is the same for all the charged particles. This was checked by turning ∇B drift on and off in the presence of $\vec{E} \times \vec{B}$ drift. Without drifts the trajectories of impurities are shown in Fig. 9(a). In the presence

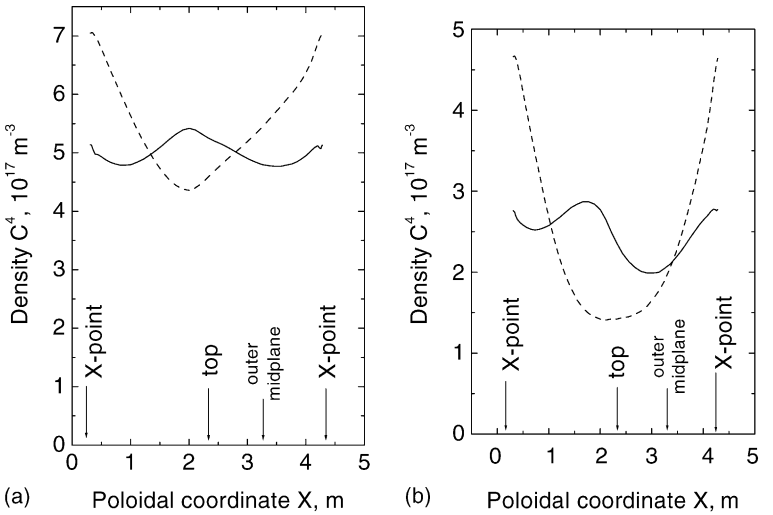

Fig. 7. Poloidal distributions for C^{4+} on the closed flux surfaces $r - a = -1.6$ cm (at the outer midplane) for different plasma temperatures, $n_e|_{-1\ cm} = 2.3 \times 10^{19}$ m^{-3}, $Z_{eff} = 1.4$. Solid lines correspond to the drifts switched on, dashed lines to the case when drifts are switched off; (a) $T_i|_{-1\ cm} = 80$ eV, (b) $T_i|_{-1\ cm} = 40$ eV.

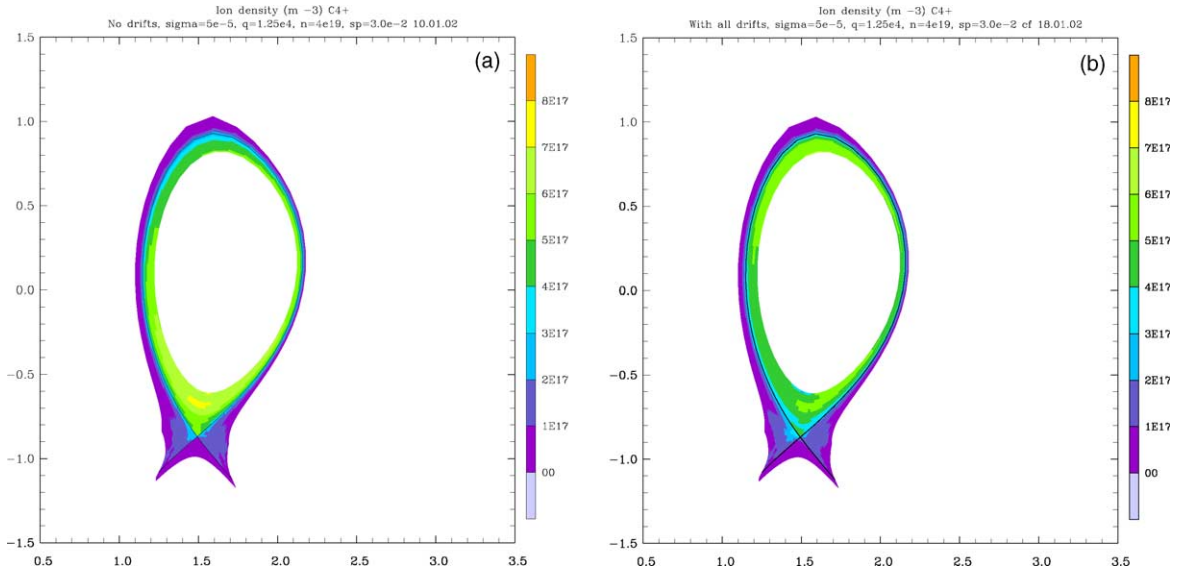

Fig. 8. Distribution of C^{4+} for the discharge parameters $P = 1$ MW, $n_e|_{-1\ cm} = 2.3 \times 10^{19}$ m^{-3}, $Z_{eff} = 1.4$; (a) without drifts, (b) with drifts.

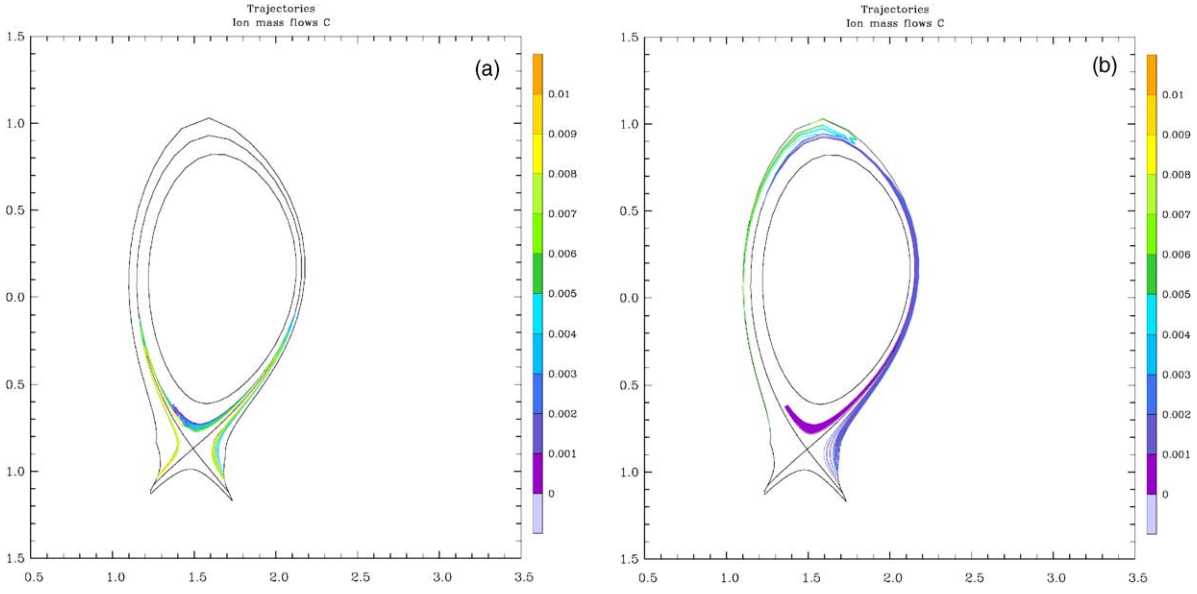

Fig. 9. (a) Trajectories of the carbon mass flow for the discharge parameters $P = 1$ MW, $n_e|_{-1\ cm} = 2.3 \times 10^{19}$ m^{-3}, $Z_{eff} = 1.4$. All drifts are switched off. Lines correspond to the trajectories of the test particles moving with the velocity averaged over all the charged carbon states. Different colors indicate time, which is necessary for particles to reach the given position (in seconds). The starting point is just above the separatrix. (b) Trajectories of the carbon mass flow. Drifts are switched on.

of $\vec{E} \times \vec{B}$ and diamagnetic drifts the trajectories of high ionized impurities are shown in Fig. 9(b). One can see that the impurities, which are ionized above the X-point on the inner flux surfaces, diffuse and rotate poloidally and are smoothed over the flux surface. The radial fluxes of the impurities are determined by the anomalous diffusion coefficients, while the neoclassical effects are very low and may be neglected.

3. Simple analytical model for high ionization states

On the closed flux surfaces the maximum of impurity density may be observed at the top or between the inner midplane and the top, Fig. 7. This effect can be understood from a simple model. Neglecting the ∇B drift of impurity ions and the effects of poloidal temperature gradient we can write the particle balance in the form:

$$\frac{\partial n_{\mathrm{I}}}{\partial t}+\frac{1}{\sqrt{g}}\frac{\partial}{\partial x}\frac{\sqrt{g}}{h_x}\left(n_{\mathrm{I}}b_z V_{\perp}^{E}+n_{\mathrm{I}}b_x V_{\mathrm{i}\parallel}-b_x^2 D_{\mathrm{I}\parallel}\frac{\partial n_{\mathrm{I}}}{h_x\partial x}\right)-\frac{1}{\sqrt{g}}\frac{\partial}{\partial y}\frac{\sqrt{g}}{h_y}\left(\frac{D_{\mathrm{I}\perp}}{T_{\mathrm{I}}}\frac{\partial n_{\mathrm{I}}T_{\mathrm{I}}}{h_y\partial y}\right)=S_{\mathrm{I}}, \tag{1}$$

where x and y axis correspond to the poloidal (clockwise) and radial directions, Fig. 1, the metric coefficients are $h_x=1/\|\nabla x\|$, $h_y=1/\|\nabla y\|$, $h_z=1/\|\nabla z\|$, $\sqrt{g}=h_xh_y\times h_z$; $b_x=B_x/B$, $b_z=B_z/B$; subscript I denotes impurity in a given ionization state, i corresponds to the background ions. The first contribution to the poloidal flux is connected with the poloidal $\vec{E}\times\vec{B}$ drift. The second term represents the motion of impurities along the magnetic field with the velocity of the background ions $V_{\mathrm{i}\parallel}$. The third term corresponds to the diffusive motion of the impurities along the magnetic field with respect to the background ions with the parallel diffusion coefficient $D_{\mathrm{I}\parallel}=T_{\mathrm{I}}/m_{\mathrm{I}}\nu_{\mathrm{Ii}}$. The radial flux is determined by the perpendicular anomalous diffusion coefficient $D_{\mathrm{I}\perp}$, the ionization source is presented in the r.h.s. In the steady-state Eq. (1) can be solved analytically when the radial diffusion is relatively slow with respect to the parallel diffusion or convection:

$$\max\left(\frac{D_{\mathrm{I}\parallel}b_x^2}{r^2},\frac{V^{(\mathrm{NEO})}}{r}\right)\gg\frac{D_{\mathrm{I}\perp}}{L_y^2}, \tag{2}$$

where r is the minor radius and L_y is the characteristic scale in the radial direction. In the second term in the l.h.s. the neoclassical expressions for the radial electric field and parallel velocity of the background ions were used [4]. Taking the neoclassical expression for the electric field in the form $\left(\langle f\rangle=\oint f\sqrt{g}\,\mathrm{d}x/\oint\sqrt{g}\,\mathrm{d}x\right)$:

$$E^{(\mathrm{NEO})}=\frac{T_{\mathrm{i}}}{e}\left(\frac{1}{h_y}\frac{\mathrm{d}\ln n_{\mathrm{i}}}{\mathrm{d}y}+k_T\frac{1}{h_y}\frac{\mathrm{d}\ln T_{\mathrm{i}}}{\mathrm{d}y}\right)-b_x\langle V_{\mathrm{i}\parallel}B\rangle,$$

where $k_T=2.7$ in the Pfirsch–Schlueter regime, we obtain (p_{i} is the pressure of the background ions):

$$V^{(\mathrm{NEO})}=b_zV_{\perp}^{E}+b_xV_{\mathrm{i}\parallel}\cong\frac{1}{en_{\mathrm{i}}B}\frac{\mathrm{d}p_{\mathrm{i}}}{h_y\,\mathrm{d}y}+(k_T-1)\frac{1}{eB}\frac{\mathrm{d}T_{\mathrm{i}}}{h_y\,\mathrm{d}y}\frac{B^2}{\langle B^2\rangle}. \tag{3}$$

The solution may be sought in the form $n_{\mathrm{I}}=n_{\mathrm{s}}(y)+\delta n(x,y)$, $n_{\mathrm{s}}\gg\delta n$ where $n_{\mathrm{s}}=\langle n_{\mathrm{I}}V^{(\mathrm{NEO})}B^2/\ B_x\rangle/\langle V^{(\mathrm{NEO})}B^2/B_x\rangle$. If the second term in Eq. (3) is negligible, n_{s} coincides with $\langle n_{\mathrm{I}}\rangle$.

The Eq. (1) yields

$$-\frac{1}{\sqrt{g}}\frac{\partial}{\partial x}\frac{\sqrt{g}}{h_x}\left(b_x^2D_{\mathrm{I}\parallel}\frac{\partial n_{\mathrm{I}}}{h_x\partial x}\right)+\frac{1}{\sqrt{g}}\frac{\partial}{\partial x}\frac{\sqrt{g}}{h_x}\left(n_{\mathrm{I}}V^{(\mathrm{NEO})}\right)=S_{\mathrm{I}}+\frac{1}{\sqrt{g}}\frac{\partial}{\partial y}\frac{\sqrt{g}}{h_y}\left(\frac{D_{\mathrm{I}\perp}}{T_{\mathrm{I}}}\frac{\partial n_{\mathrm{s}}T_{\mathrm{I}}}{h_y\partial y}\right). \tag{4}$$

Integrating Eq. (4) over the flux surface provide the equation for $n_{\mathrm{s}}(y)$:

$$-\frac{\partial}{\partial y}\left(\frac{\partial n_{\mathrm{s}}T_{\mathrm{I}}}{\partial y}\oint\frac{\sqrt{g}}{h_y^2}\frac{D_{\mathrm{I}\perp}}{T_{\mathrm{I}}}\,\mathrm{d}x\right)=\oint\sqrt{g}S_{\mathrm{I}}\,\mathrm{d}x. \tag{5}$$

The equation for poloidal distribution of impurities may be obtained from Eq. (4):

$$\frac{\partial\delta n}{h_x\partial x}-\frac{V^{(\mathrm{NEO})}}{b_x^2D_{\mathrm{I}\parallel}}\delta n=\frac{1}{B_xD_{\mathrm{I}\parallel}}n_{\mathrm{s}}\left[V^{(\mathrm{NEO})}\frac{B^2}{B_x}-\left\langle V^{(\mathrm{NEO})}\frac{B^2}{B_x}\right\rangle\frac{B^2}{\langle B^2\rangle}\right]-\frac{1}{B_x}\left[f(x)-\langle f(x)\rangle\frac{B^2}{\langle B^2\rangle}\right], \tag{6}$$

where

$$f(x)=\frac{B^2}{D_{\mathrm{I}\parallel}}\int_{x_0}^{x}\frac{1}{B_x}\left[S_{\mathrm{I}}+\frac{1}{\sqrt{g}}\frac{\partial}{\partial y}\frac{\sqrt{g}}{h_y}\left(\frac{D_{\mathrm{I}\perp}}{T_{\mathrm{I}}}\frac{\partial n_{\mathrm{s}}T_{\mathrm{I}}}{h_y\partial y}\right)\right]h_x\,\mathrm{d}x.$$

To understand qualitatively the behavior of δn, Eq. (6) is solved in the high aspect ratio case for the tokamak with a circular cross-section, with the assumption that the second term in Eq. (3) is small:

$$n_{\mathrm{I}}=\langle n_{\mathrm{I}}\rangle\left(1+\frac{2\varepsilon A}{\sqrt{A^2+1}}\sin(\theta-\varphi)\right)-\int_0^{\theta}\frac{r}{B_x}\left[f(\theta')-\langle f(\theta')\rangle\frac{B(\theta')^2}{\langle B^2\rangle}\right]\exp(A\theta-A\theta')\,\mathrm{d}\theta'+\frac{1}{1-\exp(-2\pi A)}\oint\frac{r}{B_x}\left[f(\theta')-\langle f(\theta')\rangle\frac{B(\theta')^2}{\langle B^2\rangle}\right]\times\exp(A\theta-A\theta')\,\mathrm{d}\theta', \tag{7}$$

where $\varepsilon=r/R$, R is the major radius, θ is the poloidal angle counted from the outer midplane (in the counter-clockwise direction), $\varphi=\mathrm{arctg}(A)$,

$$f(\theta)=\frac{B^2}{D_{\mathrm{I}\parallel}}\int_0^{\theta}\frac{1}{B_x}\left[S_{\mathrm{I}}+\frac{1}{rR}\frac{\partial}{\partial r}rR\left(\frac{D_{\mathrm{I}\perp}}{T_{\mathrm{I}}}\frac{\partial\langle n_{\mathrm{I}}\rangle T_{\mathrm{I}}}{\partial r}\right)\right]r\,\mathrm{d}\theta'.$$

The second and third terms in r.h.s. of Eq. (7) reflect the poloidal dependence of the radial diffusive flux due to variation of the distance between the flux surfaces and the poloidal dependence of impurity source. The average density $\langle n_{\mathrm{I}}\rangle=n_{\mathrm{s}}$ may be calculated from Eq. (5). Let us focus on the first term. The position of density maximum depends on the parameter

$$A=\frac{V^{(\mathrm{NEO})}r}{b_x^2D_{\mathrm{I}\parallel}}\approx Z\frac{r}{L_y}\frac{B^2}{B_x^2}\frac{\nu_{\mathrm{Ii}}}{\omega_{\mathrm{cI}}}.$$

Here Z is the impurity charge number, ν_{Ii} and ω_{cI} are the collision frequency and cyclotron frequency for impurity ions, $V^{(\mathrm{NEO})}=-(1/en_{\mathrm{i}}B)(\mathrm{d}p_{\mathrm{i}}/\mathrm{d}r)$ in the simplified case. The density maximum is situated near the top if $A\ll1$ and is shifted to the inner midplane if $A\gg1$. The first case corresponds to the strong parallel diffusion so that

the divergence of the poloidal rotation is compensated by the flows arising from the poloidal density gradient. In the second case the parallel diffusion is relatively small with respect to the poloidal convection and the density profile organizes so that $(\sqrt{g}/h_x)n_I V^{(NEO)} \cong$ constant.

The account of temperature variations and thermal force on the closed flux surfaces does not change qualitatively the density variation since for the parameters of simulation the thermal force does not exceed the drag of the main ions.

4. Comparison with simulation results

For discharges with sufficient additional heating with the temperature at the reference point ($a - r = 1$ cm) $T_i \approx 80$ eV the condition Eq. (2) is satisfied. For C^{4+}, C^{5+} the first term of Eq. (7) dominates and corresponding maximum of density is more pronounced than the maximum near the X-point which is connected with the ionization source, Fig. 7(a). The intermediate maximum position agrees with the value of the parameter $A \sim 1$. For C^{5+} the parameter $A \sim Z^2$ is higher than for C^{4+}, and the maximum is more shifted to the inner midplane.

For the discharges with the smaller heating power ($T_i \approx 40$ eV) the condition Eq. (2) is not fulfilled. For such discharges the poloidal length of parallel diffusion $L_D \approx L_y\sqrt{D_{I\|}b_x^2/D_{I\perp}}$ is smaller than the poloidal length of the flux surface. As a result the poloidal impurity distribution in the absence of poloidal drifts is quite inhomogeneous, Fig. 7(b).

In this case the influence of drifts also can be estimated using the velocity $V^{(NEO)}$ of the main plasma component. The characteristic length of drifts during the time, which is necessary to diffuse in the perpendicular direction, is $L_d \approx V^{(NEO)}L_y^2/D_{I\perp}$. The density of impurities is determined by the maximal of lengths L_d, L_D and L_S, where L_S is the poloidal length of the impurity source. If the largest of these lengths is smaller than the poloidal length of the flux surface, the density profile is peaked around the impurity source, the estimate for the density is

$$\langle n_I\rangle \sim \frac{\langle S_I\rangle L_S L_y^2}{D_{I\perp}\max\{L_S, L_d, L_D\}}. \quad (8)$$

In the case of the high drift length the density is inversely proportional to the drift velocity. Our calculations for small heating power (0.4 MW, $T_i \approx 40$ eV) give the parameters $L_D \approx 1$ m, $L_S \approx 1.2$ m, $L_d \approx 2$–5 m while flux surface length is of the order of 4 m. So after the switching the drifts on we can expect the smoothening of poloidal impurity profile, Fig. 7(b).

The role of drifts is illustrated schematically by Fig. 10. Divergence of poloidal drift fluxes in inhomogeneous magnetic field produces additional effective source of impurities at the upper part of the torus. Parallel and perpendicular diffusion fluxes of impurities determine their poloidal distribution on the closed flux surface, the corresponding fluxes are shown in Fig. 10. Outside the separatrix impurities are dragged towards the plates by the background ions. As a whole $\vec{E}\times\vec{B}$ drift leads to decrease of average impurity density inside the separatrix since the more uniform distribution in the presence of drifts accelerates the impurity diffusion. This could be understood from the fact that in the presence of drifts impurities are escaping from the whole flux surface, while in the absence of drifts impurities diffuse only through the lower part of the flux surface. Since the source of C^{4+} (C^{3+}) integrated over the closed flux surface remains the same in both cases, the average density with $\vec{E}\times\vec{B}$ drifts should be lower than without drifts. In the calculations without drifts the MARFE formation occurs at the lower level of sputtering than in the calculations with the drifts switched on.

The simulations were performed with and without neutral beam injection (NBI). The toroidal rotation velocity was specified at the inner boundary. Alternatively the radial flux of toroidal momentum at the inner boundary was prescribed [4]. Average toroidal velocity up to 30 km/s at the inner boundary did not change

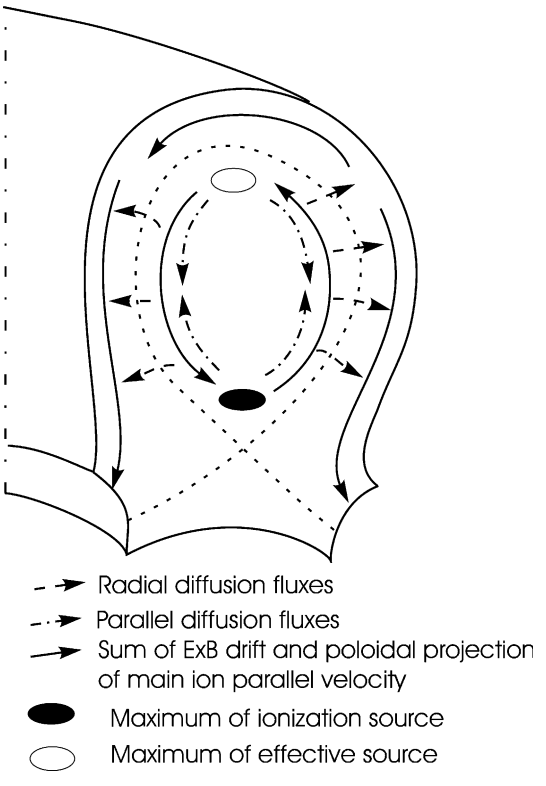

Fig. 10. Scheme of impurity fluxes near the separatrix.

significantly the poloidal distribution of impurities both on the open and closed field lines. On the closed field lines this fact can be understood from the neoclassical character of the poloidal rotation of the background ions. The toroidal rotation did not change the poloidal rotation in accordance with Eq. (3) (the contribution from the term $b_x V_{i\|}$), while the latter determines the poloidal impurity distribution on the closed flux surfaces. The variation of the poloidal profiles of C^{1+}, C^{2+}, C^{3+} outside the separatrix was of the order of 10%, which is consistent with the variation predicted in [13] for the main component. The relative density variation near the plates should be of the order of the ratio of the average toroidal rotation velocity at the separatrix to the sound speed at the plates, which in our runs did not exceed 10%.

In the simulations performed the main fluxes of neutral deuterium and carbon come from the divertor plates. However, there is experimental evidence that the neutral flux from the wall is larger than is predicted by standard simulations [14]. To check sensitivity of the results obtained to the variation of the fluxes of neutrals from the wall special runs were performed with particle diffusivity increasing in the SOL towards the wall. Different profiles of D were used with D at the wall 10 times larger than D at the separatrix. In these runs the neutral flux from the wall was 2.5 larger than in the standard runs and was of the order of 40% of the neutral flux from the divertor plates. In these runs the absolute values of impurity density change but their poloidal distribution and all patterns remain qualitatively the same as in the standard runs.

5. Conclusions

The impact of the $\vec{E} \times \vec{B}$ drifts is most pronounced inside the separatrix for impurities in high ionization states. Both poloidal $\vec{E} \times \vec{B}$ drifts of impurities and parallel drag from the background ions lead to smoother poloidal density distribution thus significantly increasing impurity density in the upper part of the torus. Diamagnetic drifts do not affect significantly the impurity distribution. The impact of the $\vec{E} \times \vec{B}$ drifts in the SOL and the PFR is more modest due to the combined effect of the poloidal drift of impurities and change of the parallel velocity of the background ions in the opposite direction.

Acknowledgements

The work was performed in the framework of German–Russian Scientific Technical Cooperation, Project RUS-00-573 and INTAS project 457. The work of group from St. Petersburg was also supported by grant RFBR 00-02-16670.

References

[1] P. Stangeby, The Plasma Boundary of Magnetic Fusion Devices, IOP, Bristol, 2000, p. 717.
[2] S.P. Hirshman, D.J. Sigmar, Nucl. Fus. 21 (1981) 1079.
[3] J. Gafert, D. Coster, C. Dorn, et al., Proceedings of the 24th EPS Conference on Controlled Fusion and Plasma Physics, v.21A Part IV (1997) 1397.
[4] V. Rozhansky, S. Voskoboynikov, E. Kaveeva, D. Coster, R. Schneider, Nucl. Fus. 41 (2001) 387.
[5] D. Morozov, V. Rozhansky, J. Herrera, K. Soboleva, Phys. Plasmas 7 (2000) 1184.
[6] V. Rozhansky, S. Voskoboynikov, E. Kaveeva, D. Coster, R. Schneider, Control. Plasma Phys. 42 (2002).
[7] A.V. Chankin, J. Nucl. Mater. 241–243 (1997) 199.
[8] A.V. Chankin et al., J. Nucl. Mater. 290–293 (2001) 518.
[9] S.K. Erents et al., Plasma Phys. Control. Fus. 42 (2000) 905.
[10] N. Asakura et al., Phys. Rev. Lett. 84 (2000) 3093.
[11] J.-L. Lachambre et al., Nucl. Fus. 34 (1994) 1143.
[12] B. Labombard, S. Gangadhara, B. Lipshultz, C.S. Pitcher, PSI-15, P2-56 (2002).
[13] V. Rozhansky, S. Voskoboynikov, E. Kovaltsova, D. Coster, R. Schneider, J. Nucl. Mater. 290–293 (2001) 710.
[14] A.Yu. Pigarov, S.I. Krasheninnikov, T.D. Rognlien, M.J. Schaffer, W.P. West, Phys. Plasmas 9 (2002) 1287.